eLife

Reviewed Preprint
v1 • May 12, 2026
Not revised

For correspondence:
eLong@nih.gov

* Scienza Health, Inc.

† AstraZeneca, Inc.

Competing interests: No competing interests declared

Funding: See page 25

Reviewing editor: Shiny Nair, Yale University, United States

Allosteric disulfide control of ligand binding and endocytosis of the natural killer cell receptor for HLA-G

Sumati Rajagopalan[1], Joyce Chiu[2,5], Jinghua Lu[3], George M Mastorakos[1,*], Saurav Majumder[1], Kristof Nolan[4,†], Erin J Adams[4], Peter Sun[3], Phillip J Hogg[2,6], Eric O Long[1]

[1]Molecular and Cellular Immunology Section, Laboratory of Immunogenetics, National Institute of Allergy and Infectious Diseases, National Institutes of Health, Rockville, United States • [2]Haematology Research Unit, School of Clinical Medicine, University of New South Wales, Sydney, Australia • [3]Structural Immunology Section, Laboratory of Immunogenetics, National Institute of Allergy and Infectious Diseases, National Institutes of Health, Rockville, United States • [4]Department of Biochemistry and Molecular Biology, University of Chicago, Chicago, United States • [5]School of Life Sciences, University of Technology Sydney, Sydney, Australia • [6]The Centenary Institute, University of Sydney, Camperdown, Australia

eLife Assessment

This study presents **important** findings on the molecular mechanisms governing how the natural killer cell receptor KIR2DL4 interacts with HLA-G and undergoes internalization. The authors provide **solid** evidence for an allosteric disulfide-bond switch that regulates receptor activity, using a multifaceted approach that includes mutagenesis, mass spectrometry, and imaging. The work would be further strengthened by validating these mechanisms in primary immune cells and providing direct structural evidence for the proposed ligand-binding interface.

https://doi.org/10.7554/eLife.111018.1.sa2

Abstract

Human Leukocyte Antigen (HLA)-G is selectively expressed by fetal trophoblast cells that invade maternal tissue and encounter maternal natural killer (NK) cells early in pregnancy. In NK cells, the endosomal receptor KIR2DL4 responds to soluble HLA-G by inducing a broad transcriptional program to support placental development. Structural features of KIR2DL4 that control ligand binding and endocytosis are unknown. Random mutagenesis revealed that three cysteines in the first immunoglobulin domain of KIR2DL4 regulated endocytosis and uptake of HLA-G. We found that the Cys10-Cys28 bond visible in the KIR2DL4 crystal structure is an allosteric disulfide with potential to switch to a Cys28-Cys74 bond. Mass spectrometry analysis showed that KIR2DL4 in human cells exists in both disulfide-bonded states. The Cys10-Cys28 bond in purified KIR2DL4 was reduced by protein disulfide isomerase (PDI) in vitro. Inhibition of PDI caused retention of KIR2DL4 at the plasma membrane and prevented HLA-G uptake. Mutants in the Cys10-Cys28 configuration endocytosed spontaneously but did not bind HLA-G. Conversely, KIR2DL4 with a Cys28-Cys74 bond was at the plasma membrane and endocytosed HLA-G. A structural change predicted by AlphaFold upon disulfide switching to the Cys28-Cys74 form reorients the D0 domain into a conformation that binds HLA-G. Thus, conversion of KIR2DL4 from an inactive state to an HLA-G binding form can regulate NK cell function to promote fetal development.

Introduction

Human natural killer (NK) cells play an important role in immune defense and reproduction (1–3). They respond to alterations in healthy cells caused by cellular stress, infections, and malignancy by killing these aberrant cells and producing cytokines and chemokines (2). In the context of pregnancy, NK cells, the most abundant lymphocyte at the maternal fetal interface, are not killers. Instead, they play a constructive role by interacting with and responding to fetal trophoblast cells. Data suggest that a secretory response by NK cells promotes remodeling of the maternal vasculature to support a successful pregnancy (4–6).

NK cells express an array of receptors to sense their environment. Integration of signals from both activating and inhibitory receptors that interact with ligands on target cells determine NK cell responses (7). The killer-cell Ig-like receptors (KIR), most of which recognize HLA class I molecules, regulate NK cell activation through expression of both inhibitory and activating KIR family members. KIR2DL4 is a unique member of the KIR family whose expression, unlike other KIR, is not limited to a subset of NK cells. KIR2DL4 has two Ig-like domains (termed D0 and D2) and activates a secretory response after engagement by a soluble agonist antibody or by soluble HLA-G (8). KIR2DL4 resides in early endosomes and binds soluble HLA-G to stimulate a broad transcriptional response, including an IFN-independent interferon stimulated gene (ISG) response in primary NK cells that may protect NK cells from pathogens (9). These responses are relevant in the context of early pregnancy where HLA-G expression by fetal trophoblast cells is controlled spatially and temporally as they invade the maternal decidua following implantation of the embryo (5).

Despite evidence of an endosomal signaling pathway initiated by a KIR2DL4–HLA-G interaction (10), direct binding of HLA-G to KIR2DL4 protein has not been reported. Even though KIR2DL4 is required for responses to HLA-G and an agonist antibody to KIR2DL4 is sufficient for activation (11, 12), the requirement for a coreceptor for HLA-G mediated activation of NK cells was not excluded. A recent study reported a strong correlation in the transcriptional response of primary NK cells stimulated with soluble HLA-G with their response to the agonist monoclonal antibody #33 (mAb #33), consistent with direct engagement of KIR2DL4 with HLA-G (9). To examine how KIR2DL4 interacts with HLA-G, we chose a random mutagenesis approach and mapped residues in the extracellular domain that are required for a physical and functional interaction with HLA-G. Several independent mutations implicated three cysteine residues in the D0 domain that controlled binding of HLA-G and endocytosis of KIR2DL4. We provide evidence for an allosteric disulfide switch between these three cysteines that regulates both endocytosis and ligand binding.

Results

Random mutagenesis of KIR2DL4 to map its interaction with HLA-G

Random mutagenesis of a cDNA fragment that encodes the KIR2DL4 extracellular domain was performed using a low-fidelity PCR reaction calibrated to generate approximately 1 to 2 base change per 1000 bp (Fig. S1A). HA-tagged KIR2DL4 with single or double amino acid changes (n=293) were transfected individually in 293T cells and examined for their ability to bind HLA-G (Fig. 1A and S1B). Transfected cells were incubated for 2 hours at 37°C with Alexa-594 coupled to an anti-HA tag antibody and with soluble HLA-G coupled to Alexa-647 (Fig. S1B). The distribution of KIR2DL4 and of HLA-G was determined by confocal microscopy (Fig. 1B). As shown previously (12), soluble HLA-G was endocytosed along with KIR2DL4 into endosomes. As controls, soluble HLA-E coupled to Alexa-647 was not bound nor internalized into KIR2DL4^{+}endosomes, and HLA-G-647 was not internalized in 293T cells expressing an HA-tagged 2B4 (*CD244*) receptor (Fig. 1B). Out of 216 clones with interpretable images of distribution at the plasma membrane or in intracellular vesicular compartments (vesicles) 153 (71%) had a phenotype that resembled wild-type KIR2DL4, leaving 63 mutants (29%) with distinct non-wild-type phenotypes (Fig. 1C).

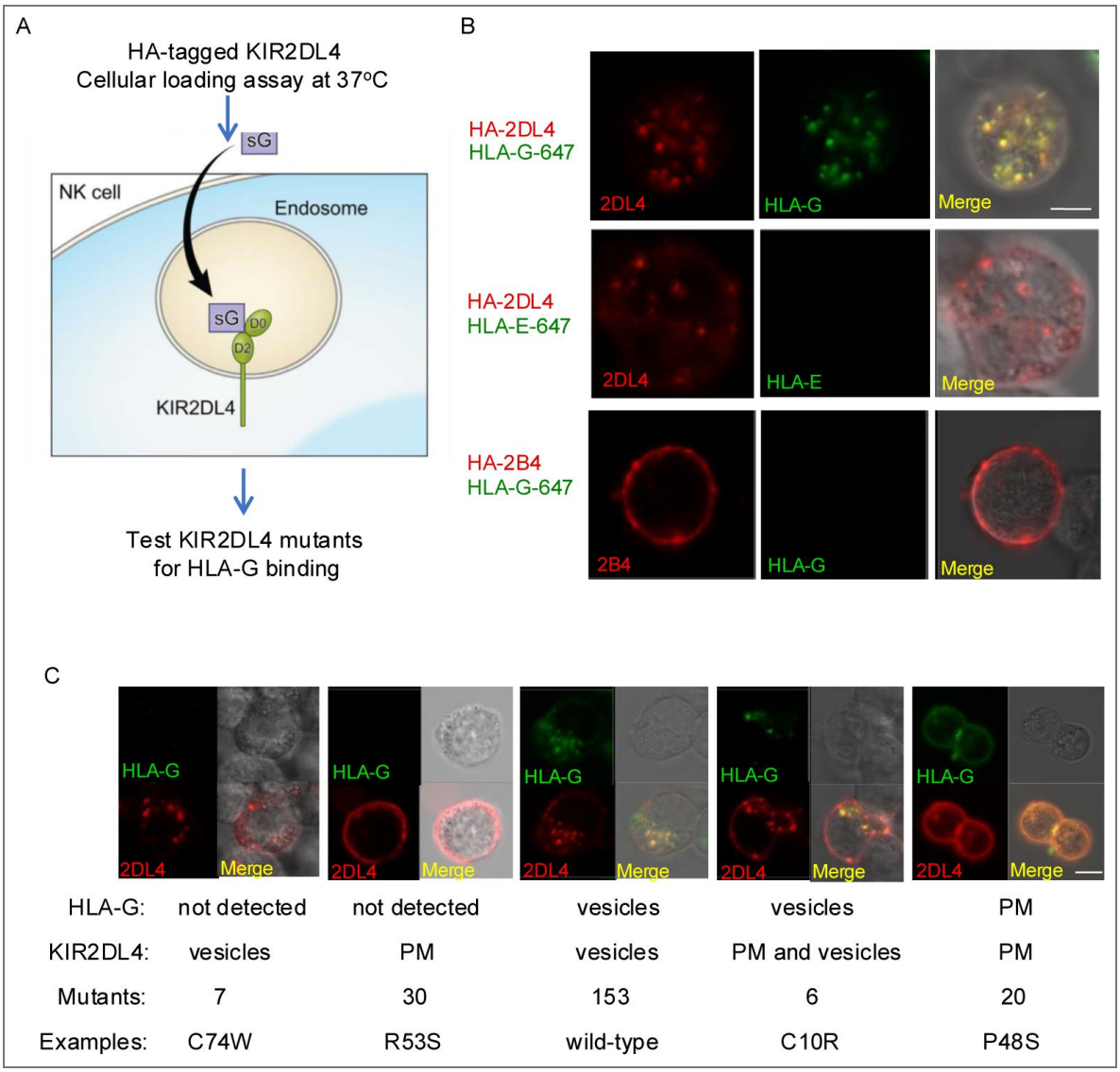

Figure 1. Random mutagenesis screen

(**A**) Soluble HLA-G (sG) is internalized with HA-tagged KIR2DL4 into endosomes, as shown by incubation for 2 h at 37°C with anti-HA coupled to Alexa-594 and soluble HLA-G coupled to Alexa-647. The loading assay was performed with 293T cells transfected with HA-tagged KIR2DL4. (**B**) Confocal microscopy showing the location of internalized KIR2DL4 (*red*) and soluble HLA-G (*green*). An overlay is shown in the right panel (*Merge*). As control, HLA-G was replaced by HLA-E, also coupled to Alexa-647 (*middle panels*). 293T cells transfected with HA-tagged receptor 2B4 were also incubated with HLA-G coupled to Alexa-647 (*bottom panels*). 2B4 (CD244) resides at the plasma membrane. (**C**) The loading assay was used to screen KIR2DL4 mutants and test for HLA-G binding. The main parameter measured was presence or absence of HLA-G and the location of detectable HLA-G. Confocal images of the five categories of mutants are shown. A DIC image is shown in the upper right panel. The parameters indicated under the images include HLA-G presence and location, location of KIR2DL4, the number of mutants in each of the five categories, and an example of a mutation for each category.

The main objective was to identify KIR2DL4 mutants that did not bind HLA-G and were otherwise in vesicles, similar to wild-type KIR2DL4 in the absence of HLA-G (12). Out of the 63 mutants, 37 failed to bind HLA-G. Only 7 of those 37 were in intracellular vesicles (Fig. 1C, *first panel*, Dataset S1). The more common phenotype of KIR2DL4 mutants that did not bind HLA-G (30 out of 37) was an even distribution at the plasma membrane (Fig. 1C, *second panel*). Mutations with that phenotype were distributed throughout the D0 and D2 Ig domains (Dataset S1), consistent with internalization into vesicles that is controlled by the KIR2DL4 extracellular domain.

Two distribution patterns were observed among the 26 mutants that bound HLA-G. Six mutants displayed a hybrid phenotype: colocalization of HLA-G with KIR2DL4 in vesicles, like wild-type, but with some KIR2DL4 remaining the plasma membrane (Fig. 1C, *fourth panel*), suggesting that internalization of these 6 mutants was facilitated by HLA-G. To test this, these mutants were examined in the absence of HLA-G. Results showed that, indeed, they remained at the plasma membrane (Fig. S1C). The other 20 mutants were detected at the plasma membrane along with HLA-G (Fig. 1C, *right most panel*). Overall, these results showed that 50 out of 63 mutants with a non-wild type phenotype (Dataset S1) failed to internalize, reinforcing the evidence that KIR2DL4 internalization is controlled by the extracellular domain (13).

The KIR2DL4 D0 domain includes 3 cysteines at positions 10, 28, and 74. Among the 7 mutants that did not bind HLA-G but resided in vesicles, two included a mutation at Cys74, such as C74W (Fig. 1C). This suggested that KIR2DL4 with a Cys10-Cys28 disulfide bond, as seen in the KIR2DL4 crystal structure (14), does not bind HLA-G but is otherwise distributed in vesicles like wild-type KIR2DL4 (12). Conversely, out of the 6 mutants with a hybrid phenotype, namely distribution at the plasma membrane and in vesicles but colocalization with HLA-G in vesicles only, one had a mutation at Cys10 (C10R). This observation showed that KIR2DL4 with the alternate bond, Cys28-Cys74, is detectable at the plasma membrane in the absence of HLA-G (Fig. S1C, left). This C10R mutant was at the plasma membrane only, demonstrating that its internalization was facilitated by soluble HLA-G. Conversely, we tested if KIR2DL4 mutants retained at the plasma membrane with bound HLA-G, such as P48S (Fig. 1C), could internalize on their own. In the absence of HLA-G, mutant P48S was in vesicles (Fig. S1C, *right*), showing that, in this case, HLA-G binding caused retention at the plasma membrane. Several targeted mutations were generated to confirm these results. The phenotypes of mutants C74W and C10R (Fig. 1C) were reproduced with targeted mutations C74R and C10S, respectively (Fig. S1D). These mutations also supported the conclusion that KIR2DL4 with a Cys28-Cys74 bond is detectable at the plasma membrane in the absence of HLA-G. Conversely, HLA-G prevented the internalization of KIR2DL4 mutants, such as P48S which otherwise endocytosed spontaneously.

An allosteric disulfide bond in KIR2DL4

The impact of cysteine mutations on the localization of KIR2DL4 led us to compare its sequence with that of other D0 domains, in KIR2DL5 and the KIR3D family (Fig. 2A). The cysteine at position 10 of KIR2DL4 is absent in these other KIRs, which have a leucine at that position. The single disulfide bond in those D0 domains is a canonical Ig domain *trans*-beta sheet bond (15), comparable to the Cys28-Cys79 bond in D1 Ig domains (Fig. 2B). Of the three potential disulfide bonds (Cys10-Cys28, Cys28-Cys74, and Cys10-Cys74), the one visible in the KIR2DL4 crystal structure (14) is Cys10-Cys28, leaving a free Cys at position 74 (Fig. 2C).

Disulfide bonds that contribute to protein folding and stabilization tend to be inert and are referred to as structural bonds (15). Labile disulfide bonds that can switch to a reduced form and back to the oxidized bond regulate protein function or localization and are referred to as allosteric bonds (15). Such bonds may be stressed and prone to cleavage (16). Formation of disulfide bonds may be reversed in reducing conditions or by the enzymatic activity of protein disulfide isomerases (PDI). Examination of the Cys10-Cys28 bond in the D0 domain of KIR2DL4, visible in the crystal structure (14), revealed that the second cysteine, Cys28, was partially exposed to solvent (Fig. 2B), compatible with a propensity for thiol disulfide exchange. By comparison, the disulfide bond in the KIR3DL1 D0 domain (Fig. 2B) is not solvent accessible, according to the crystal structure (17). Given that KIR2DL4 may be regulated by an allosteric disulfide bond, we examined

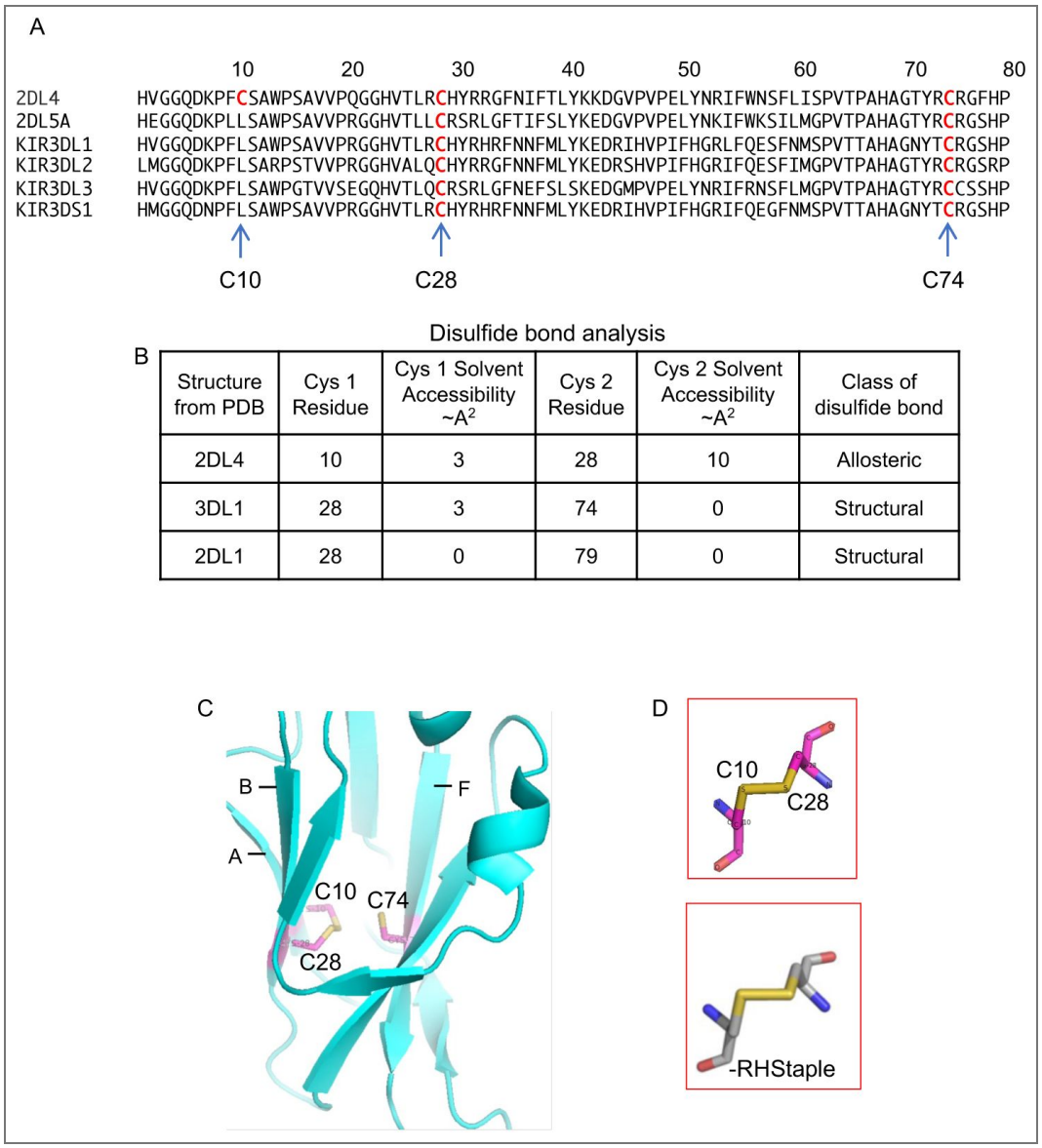

Figure 2. A stressed disulfide bond typical of an allosteric bond in the crystal structure of KIR2DL4

(**A**) The KIR2DL4 D0 domain has a third Cys residue not found in other D0 domains. Sequence alignment of D0 domains with Cys residues indicated by an arrow and shown in red (**B**) Disulfide bonds visible in crystal structures of KIRs exhibit a higher solvent accessibility in the Cys10-Cys28 bond unique to KIR2DL4. Solvent accessibility of disulfide bonds was determined by DSSP (define secondary structure of proteins) algorithm. (**C**) Position of the three Cys residues in the crystal structure of KIR2DL4 (3WYR). Cys10, Cys28 and Cys74 are on the A strand, B strand and F strands, respectively, are as indicated. (**D**) The disulfide bond configuration in the KIR2DL4 D0 domain is an –RHstaple.

the configuration of the Cys10-Cys28 disulfide (Fig. 2C). Among the 20 possible disulfide bond conformations, as determined by the geometry of the five dihedral angles that describe the cysteine residue, three of them are characteristic of allosteric bonds (15, 18). The Cys10-Cys28 bond in the KIR2DL4 structure has an archetypal –RHstaple allosteric conformation (Fig. 2D), which is characterized by high tensile pre-stress due to stretching of the S-S bond and neighboring α angles (19).

Disulfide bonds in KIR2DL4

As cysteine mutations in the D0 domain of KIR2DL4 had an impact on internalization and cellular distribution, we determined what disulfide bond out of the three possible (Cys10-Cys28, Cys28-Cys74, and Cys10-Cys74) (Fig. 3A) existed in recombinant KIR2DL4 produced in insect cells. Cysteine pairings for disulfide bonds in recombinant KIR2DL4 were mapped using disulfide-linked peptides and mass spectrometry. The conserved Cys123-Cys172 bond in domain D2 (Fig. 3A) served as a reference. In wildtype KIR2DL4, peptides linked by disulfides Cys10-Cys28, Cys10-Cys74, Cys28-Cys74 from D0 and Cys123-Cys172 from D2 were identified and quantified (Fig. 3A and B; Fig. S2). Cys10-Cys28 represented the most abundant bond in D0 and as expected, was abundant in the C74S mutant but absent in the C10S mutant (Fig. 3B). The recovery of the reference Cys123-Cys172 bond in the D2 domain was lower (approximately one third) but, as expected, its abundance was virtually identical in the 3 isoforms of KIR2DL4 (wild-type, C10S, and C74S). The Cys28-Cys74 bond in D0 was detected at a lower abundance than Cys10-Cys28, and as expected, was more abundant in the C10S mutant (Fig. 3B). The Cys10-Cys74 bond was detected at a low abundance and was completely absent in the C10S and the C74S mutants (Fig. 3B). In conclusion, wild-type purified KIR2DL4 existed in both configurations, Cys10-Cys28 and Cys28-Cys74, representing independent isoforms distinguished by their disulfide bond in the D0 domain Fig. 3B).

The redox state of cysteines in KIR2DL4 purified from insect cells was then determined by differential cysteine alkylation and mass spectrometry (Fig. 3C; Table S1). Unpaired or reduced cysteines were first labelled with the cysteine alkylator ^{12}C-IPA. Disulfide bonds were then reduced by dithiothreitol followed by cysteine alkylation with ^{13}C-IPA. The fraction of reduced disulfide bonds was measured from the relative ion abundance of peptides containing ^{12}C-IPA or ^{13}C-IPA (Fig. 3C). By this approach, the relative abundance of reduced cysteines in wild-type KIR2DL4 was 32.3%, 4.5%, and 74.3% for Cys10, Cys28, and Cy74 respectively (Fig. 3D). Based on these measurements, the calculated abundance of Cys10-Cys28 and Cys28-Cys74 was 67.7% and 25.7%, respectively. This data demonstrated that these two disulfide forms exist in the D0 domain.

Next, we tested if the Cys10-Cys28 and Cys28-Cys74 disulfide pairs existed in KIR2DL4 obtained from human cells, using the same protocol as in Fig. 3C and 3D with the following modifications. Unpaired cysteines on intact 293T-2DL4-gfp cells were first labelled with ^{12}C-IPA, followed by cell lysis, pull-down of KIR2DL4 via the GFP tag, and a second labelling with ^{12}C-IPA prior to elution. Eluted proteins were separated by gel electrophoresis and those with an approximate mass of 75 kD were isolated. Disulfide bonds were then reduced and the new unpaired cysteines alkylated, this time with ^{13}C-IPA (Fig. 3C). The redox states of cysteines were quantified by mass spectrometry analysis. The fraction of reduced disulfide bonds was calculated from the relative ion abundance of peptides containing ^{12}C-IPA and ^{13}C-IPA (Fig. 3C). The Cys10-Cys28 and the Cys28-Cys74 forms of KIR2DL4 were detected at a 48.15% and 35.04% relative abundance, respectively (Fig. 3E). A KIR2DL4 in the Cys10-Cys74 configuration was not detected, consistent with the very low abundance of reduced Cys28 in recombinant KIR2DL4 (Fig. 3D). The structural Cys123-Cys172 bond in the D2 Ig domain, was present at an 82.96% relative bonded state, equivalent to the total bonded state of the D0 domain (48% + 35%). We concluded that wild-type KIR2DL4 expressed in human cells exists in both disulfide forms (Cys10-Cys28 and Cys28-Cys74), supporting the possibility of an allosteric transition between the two.

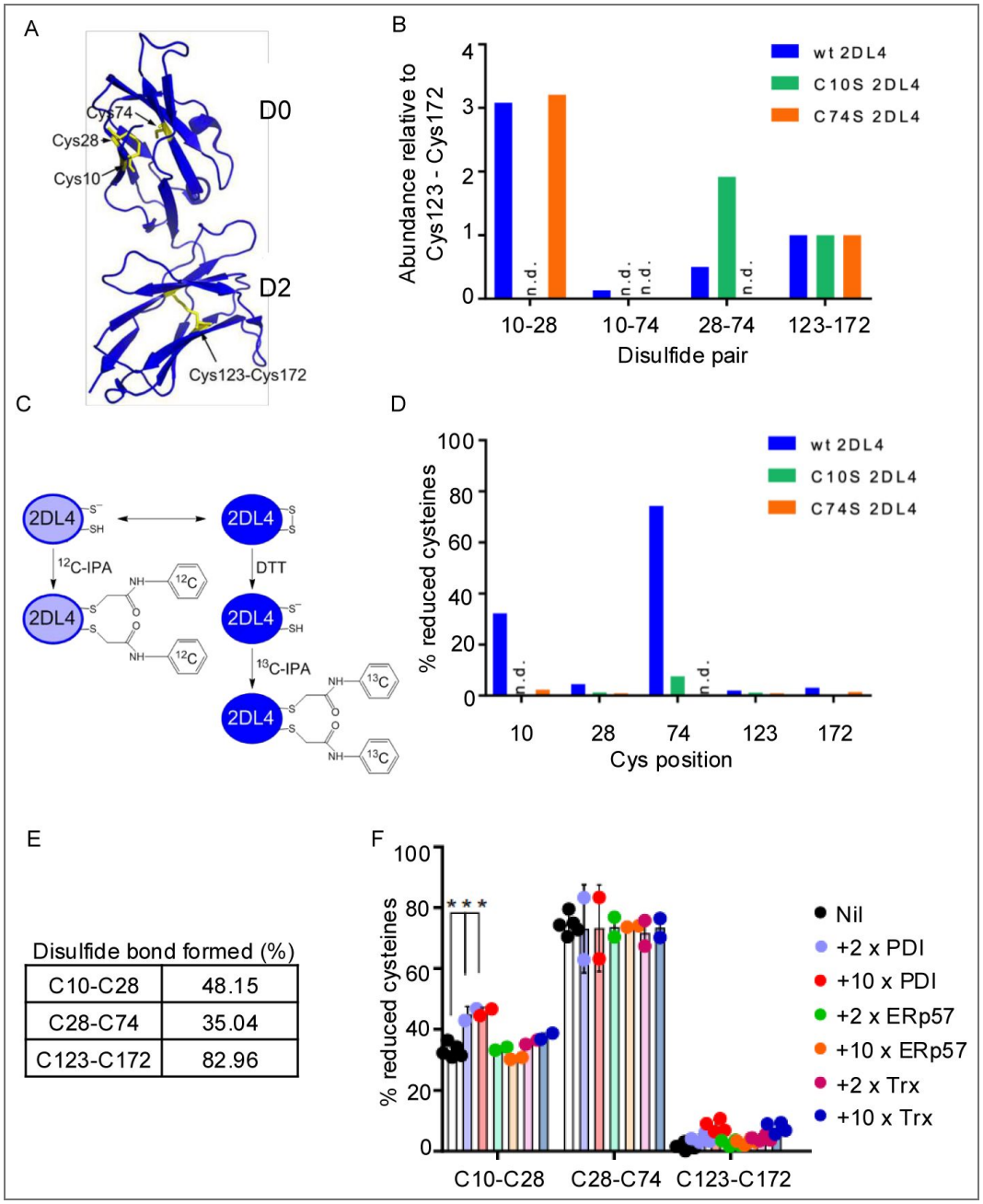

Figure 3. Detection and quantification of disulfide bonds in KIR2DL4 isolated from cells

(**A**) Disulfide bonds in KIR2DL4. The Cys10-Cys28 disulfide bond and the unpaired Cys74 in the D0 domain and the stable Cys123-Cys172 disulfide bond in the D2 domain are shown in yellow in the ribbon structure of KIR2DL4. PDB identifier is 3WYR. (**B**) Quantification of disulfide-linked peptides in recombinant KIR2DL4 by mass spectrometry. Peptide abundance was expressed relative to the peptide linked by Cys123 and Cys172 in D2 of the receptor. (**C**) Protocol to determine the redox state of KIR2DL4 disulfide bonds, as measured by differential cysteine alkylation and mass spectrometry. Reduced disulfide bond cysteines in KIR2DL4 were alkylated with ^{12}C-IPA and the oxidized cysteine thiols with ^{13}C-IPA following reduction with DTT. The ratio of ^{12}C-IPA to ^{13}C-IPA alkylation represents the proportion of the disulfide bonds in the population that are in the reduced state. (**D**) Quantification of cysteine redox states in recombinant KIR2DL4 by differential cysteine alkylation and mass spectrometry. **(E)** Human cell-derived KIR2DL4 was found in both Cys10-Cys28 and Cys28-Cys74 redox states. The redox state of disulfide Cys123-Cys172 is shown for comparison. (**F**) Incubation of purified KIR2DL4 with 3 different protein disulfide isomerases. Reduction of the Cys10-Cys28 bond occurred with PDI at a molar ratio of 2 and 10. The redox state of cysteines were quantified by differential cysteine labelling and mass spectrometry. The error bars (SD) were derived from measurements of 2 to 4 peptides. ***<0.005 as assessed by unpaired, two-tailed Students t-test.

Protein disulfide isomerase controls endocytosis of KIR2DL4

Given that the disulfide-bonded Cys28 in the KIR2DL4 crystal structure is partially exposed to solvent (Fig. 2B), we tested if it was sensitive to cleavage by thiol isomerases. Recombinant KIR2DL4 isolated from insect cells was incubated with the three reduced thiol isomerases PDI (*PDIA1*), Erp57 (*PDIA3*), and thioredoxin (*TXN*). Significant reduction of the Cys10-Cys28 bond but not the Cys28-Cys74 bond was observed in the presence of PDI, but not the other two isomerases (Fig. 3F). Therefore, reduction of Cys10-Cys28 by PDI revealed a selectivity at two levels. One is that the Cys28-Cys74 was resistant, suggesting that the Cys10-Cys28 bond is more accessible to PDI. Second, the lack of reduction by the two other isomerases, Erp57 and Thioredoxin, suggested that accessibility of the Cys10-Cys28 bond to these isomerases is limited.

So far, our results, including data obtained with an unbiased mutagenesis screen, pointed to a major role of disulfide bonds in the D0 domain for KIR2DL4 trafficking and to regulation by the activity of protein disulfide isomerase. Several PDI inhibitors were used to examine the cellular distribution of HA-tagged KIR2DL4 in 293T cells incubated with soluble HLA-G coupled to a fluorophore. Two types of inhibitors were used. The first consisted of two thiol blockers that interact irreversibly with free and exposed thiol groups (DTNB and pCMPS). In untreated cells, KIR2DL4 was found mostly in endocytic vesicles together with soluble HLA-G (Fig. 1B and Fig. 4, *first panels*). In transfected cells with a high level of KIR2DL4 expression, some KIR2DL4 was detected at the plasma membrane. With increasing concentrations of DTNB (Fig. 4A) or pCMPS (Fig. 4B), the proportion of cells exhibiting KIR2DL4 at the plasma membrane increased. Uptake of HLA-G was sensitive to DTNB and, to a lesser extent, with pCMPS.

Incubation with rutin (quercetin-3-rutinoside), a selective inhibitor of PDI that does not inhibit other extracellular thiol isomerases present in the vasculature (20), had a similar effect as thiol blockade (Fig. 4C). Blocking of PDI with a specific antibody inhibited internalization of KIR2DL4 but not as efficiently as thiol blockers (Fig. 4D). Thus, blocking the activity of PDI with inhibitors and PDI blockade with an antibody prevented endocytosis of KIR2DL4 and reduced the binding of HLA-G to KIR2DL4.

Disulfide bonds in KIR2DL4 regulate binding to HLA-G and endocytosis

To further evaluate the role of alternative disulfide bonds in the D0 domain and for a comparison of the same cysteine substitutions, each one of the three cysteines in the D0 domain was replaced with a serine. The C10S and the C28S mutants remained mostly at the plasma membrane (Fig 5A), indicating that a Cys28-Cys74 configuration or a Cys10-Cys74 configuration (if it were to exist) did not internalize into vesicles. Conversely, the C74S mutant, which is limited to a Cys10-Cys28 bond, was distributed in intracellular vesicles nearly as much as wild-type KIR2DL4 (Fig. 5A).

Considering that HLA-G bound to KIR2DL4 in a Cys28-Cys74 configuration, several mutants of Cys10 were tested for their ability to bind HLA-G and internalize. Three substitutions of Cys10 in HA-KIR2DL4 (C10R, C10S and C10A) transfected into 293T cells were able to bind HLA-G and to internalize as well as wild-type (Fig. 5B). There was very little internalization of HA-KIR2DL4 into vesicles without concomitant uptake of HLA-G (Fig. 5B), as was seen with wild-type KIR2DL4 (Fig. 1B). Therefore, KIR2DL4 with a Cys28-Cys74 disulfide bond behaved as wild-type as far as HLA-G binding and transport to intracellular vesicles was concerned but failed to internalize on its own. A summary of cysteine mutants and their impact on KIR localization and interaction with HLA-G is shown in Table 1.

The X-ray crystal structure of a KIR2DL4 that had been produced and purified from human cells (14) revealed an unexpected cross-strand Cys10-Cys28 bond in D0, rather than the canonical cross-β sheet Cys28-Cys74 (Fig. 5C). By comparison, AlphaFold2, a deep learning based prediction tool to model a protein's 3D structure from its amino acid sequence (21, 22), predicted a KIR2DL4

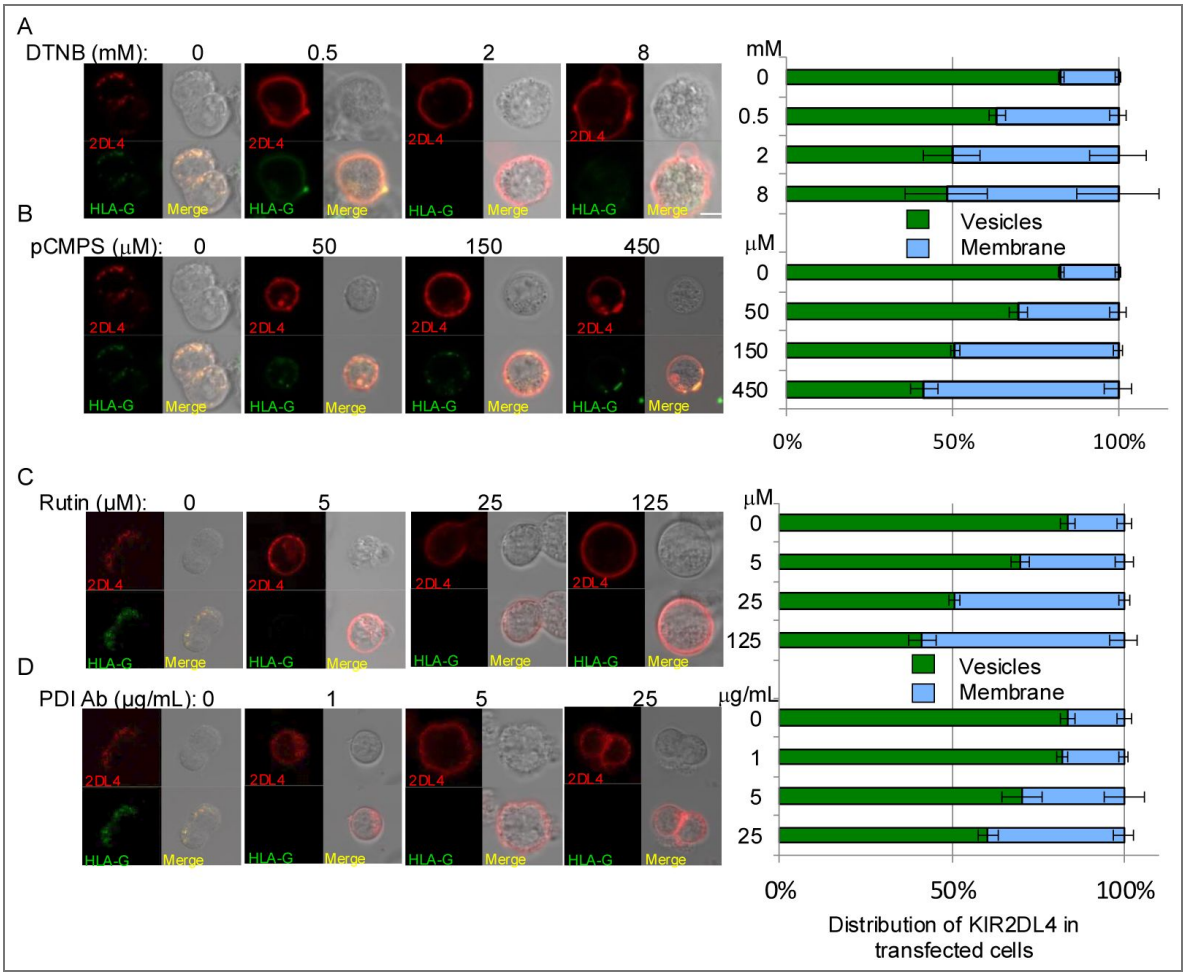

Figure 4. Location of KIR2DL4 and HLA-G after inhibition of PDI

(**A** to **D**) Confocal microscopy images of 293T cells transfected with HA-KIR2DL4 (anti-HA coupled to Alexa 594, *red*) and loaded with labeled HLA-G (*green*) for 2 h in the presence of DTNB (**A**), pCMPS (**B**), Rutin (**C**) and anti-PDI antibody (**D**), at the indicated concentrations. The time 0 image in (A) and (B) is the same, and so is the time 0 image shown in (C) and (D). The distribution of KIR2DL4 in vesicles or on the cell surface was determined by scoring at least 200 cells per condition.

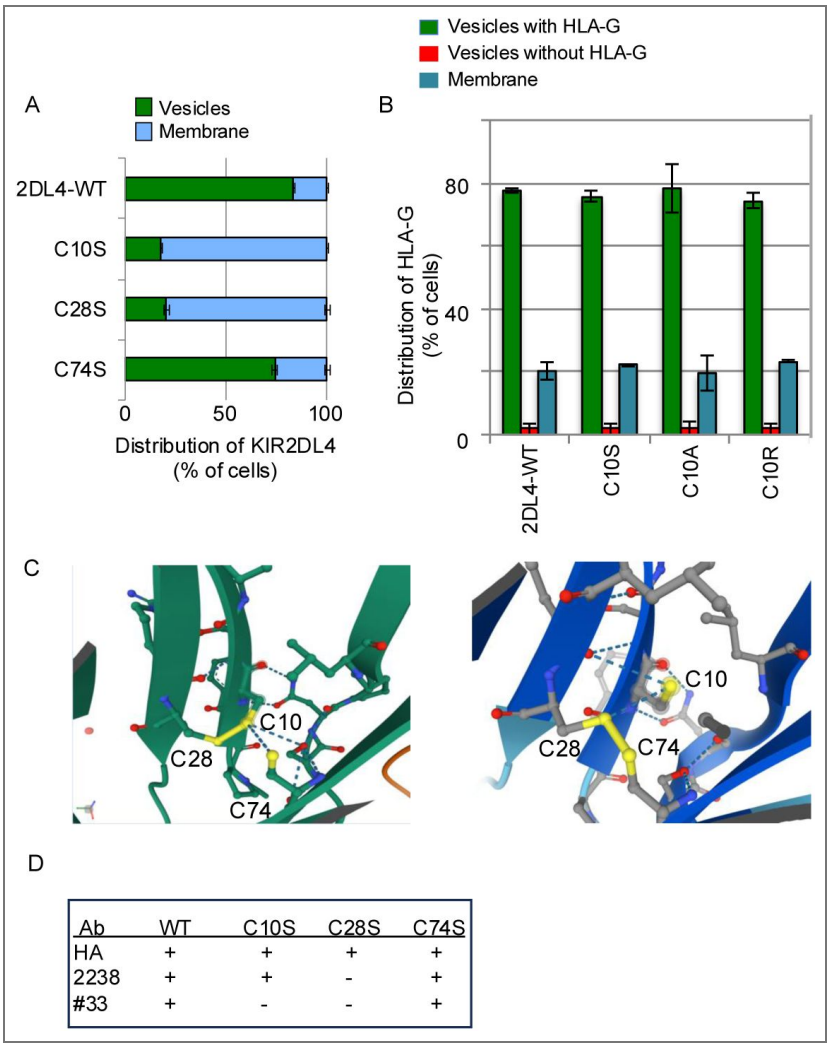

Figure 5. Cysteine mutants in KIR2DL4 tested for their impact on KIR2DL4 distribution

(**A**) Distribution (vesicles or plasma membrane) of WT and of the indicated cysteine mutants of KIR2DL4 in transfected 293T cells. (**B**) Distribution of HLA-G in 293T cells transfected with KIR2DL4 wild-type and with mutations at Cys10. HLA-G was scored for presence or absence in KIR2DL4+ vesicles. (**C**) Close-up view of the trio of cysteines in the D0 domain of KIR2DL4, as reported in the crystal structure (3WYR, *left*) and as predicted by AlphaFold (*right*). (**D**) Reactivity of the antibodies anti-HA tag, mAb#33 and MAB2238 with wild-type and the 3 cysteine mutants of KIR2DL4.

KIR2DL4 Cys mutants	KIR2DL4 location	KIR2DL4 location upon sHLA-G load	sHLA-G location	Disulfide Bonds in D0 domain
WT	V	V	V	3 possible
C10S	PM	PM and V	V	C28-C74
C10A	PM	PM and V	V	
C10R	PM	PM and V	V	
C28S	PM	PM	None	C10-C74
C28A	PM	PM	None	
C28R	PM	PM	None	
C74S	V; some PM	V	Few V	C10-C28
C74A	V	V	None	
C74R	V	V	Few V	
C74W	V	V	None	

Table 1. Cysteine mutants in the D0 domain of KIR2DL4 and their impact on the distribution of KIR2DL4 and its interaction with HLA-G.

V=vesicular; PM=Plasma membrane.

structure with a Cys28-Cys74 bond (Fig. 5C), supporting the notion that KIR2DL4 can exist in both configurations and consistent with an allosteric transition between two disulfide bonded states.

The agonist mAb #33 and the antibody MAB2238 to KIR2DL4 were tested for binding with the three different Cys mutations. As control, an antibody to the HA-tag fused to the extracellular N-terminus of KIR2DL4 was used (Fig. 5D, Fig. S2). Neither mAb #33 nor MAB2238 bound to the C28S mutant, likely to be misfolded due to the lack of a Cys10-Cys74 disulfide bond, as shown by mass spectrometry. While they both bound to the C74S mutant, limited to a Cys10-Cys28 bond, only MAB2238 bound to the C10S mutant, limited to a Cys28-Cys74 bond (Fig. 5D). Therefore, mAb #33 does not recognize KIR2DL4 in a Cys28-Cys74 configuration and binds selectively to the Cys10-Cys28 disulfide bonded state (Fig. 5D and Fig.S3).

HLA-G binding is controlled by an allosteric disulfide in the KIR2DL4 D0 domain

Alpha-Fold2 (21, 22) predicted a KIR2DL4 structure in the Cys28-Cys74 disulfide-bonded form (Fig. 6A), rather than the Cys10-Cys28 configuration in the crystal structure (14). This is consistent with the two configurations of KIR2DL4 that we identified biochemically using differential cysteine labeling and mass spectrometry (Fig. 3E). An overlay of these two structures, the PDB 3WYR structure (purple) and the AlphaFold prediction (blue), revealed differences in the D0 domain. Besides the difference in the disulfide bond, a loop that follows the β-strand C with two prolines at position 46 and 48 was clearly different (Fig. 6A, *blue arrow*, and Fig. 6B). This loop is located near the D2 domain (Fig. 6A) at a point similar to the “elbow” formed by domains D1 and D2 of KIR2D receptors and where HLA-C binds (23, 24). The different orientation of the P46 side chain in the two structures is not due to proline isomerization, as prolines P46 and P48 are in a trans configuration in both structures. The conformation predicted by AlphaFold2 for KIR2DL4 in the Cys28-Cys74 bonded form showed a 5.4 Å distance between the side chain of P46 with that of the crystal structure, and a 5.3 Å distance for the side chain of V45 (Fig. 6B).

AphaFold3, a predictor of the structure of protein complexes, revealed a potential interaction between HLA-G and KIR2DL4 in a Cys28-Cys74 configuration (Fig. 6C; Fig. S4A). Contacts with HLA-G were apparent in D0 at Val45 and Pro48, two residues within the predicted loop that distinguishes the two disulfide bonded states of KIR2DL4 (Fig. 6C). Val45 and Pro48 were predicted to form bonds with Met76 and Glu19 of HLA-G, respectively (Fig. 6C). Met76 is unique to HLA-G, as it is different in other human HLA-I (25). Position 76 is a Glu in HLA-B, which contacts KIR3DL1 at Ala167 in the D1 domain (17). Several predicted interactions occurred in the more conserved D2 domain, present in all KIR2D and KIR3D receptors. Four amino acids within a 7-amino acid long stretch in HLA-G (R145 to N151) could provide contacts with 6 amino acids in the D2 domain of KIR2DL4. Arg145 in HLA-G contacts Ser128 and Asp130 of KIR2DL4, and Lys146 contacts Ser179 in the C28-C74 disulfide bonded KIR2DL4 (Table S2). In addition, Ala149-Ala150-Asn151 in HLA-G are predicted to contact the 3 consecutive residues, Leu99-Tyr100-Glu101 (Table S2), which is conserved in the D2 domains of KIR2DL4, KIR2DL1, and KIR3DL3.

In the case of a Cys10-Cys28 configuration, as seen in the crystal structure, the V45 to P48 residues are predicted to be too distant from the Met76 and Glu19 of HLA-G, which contact KIR2DL4 in a Cys28-Cys74 configuration (Fig. 6C and D; Fig. S4A and B). Notably, the structure predicted by AlphaFold for a C74R mutant (limited to a Cys10-Cys28 disulfide bond) is very similar to that of the KIR2DL4 crystal structure and is also too distant from HLA-G for an interaction (Fig. 6E; Fig. S4C). Consistently, the structure of a C10R mutant (limited to a Cys28-Cys74 bond) is compatible with similar contacts with HLA-G as those predicted by AlphaFold for a wild-type KIRDL4 in a Cys28-Cys74 configuration (Fig. 6F; Fig. S4D). The conformational change in the Pro46-Pro48 loop, which clearly distinguishes the two forms of KIR2DL4, the Cys10-Cys28 from the Cys28-Cys74 configurations, is in the portion of the D0 domain sequence with the widest divergence from D0 domains of other KIR. In the nine amino acid stretch G44 to N52 (GVPVPELYN), only P48 is shared with 3DL1 and 3DL2 sequences.

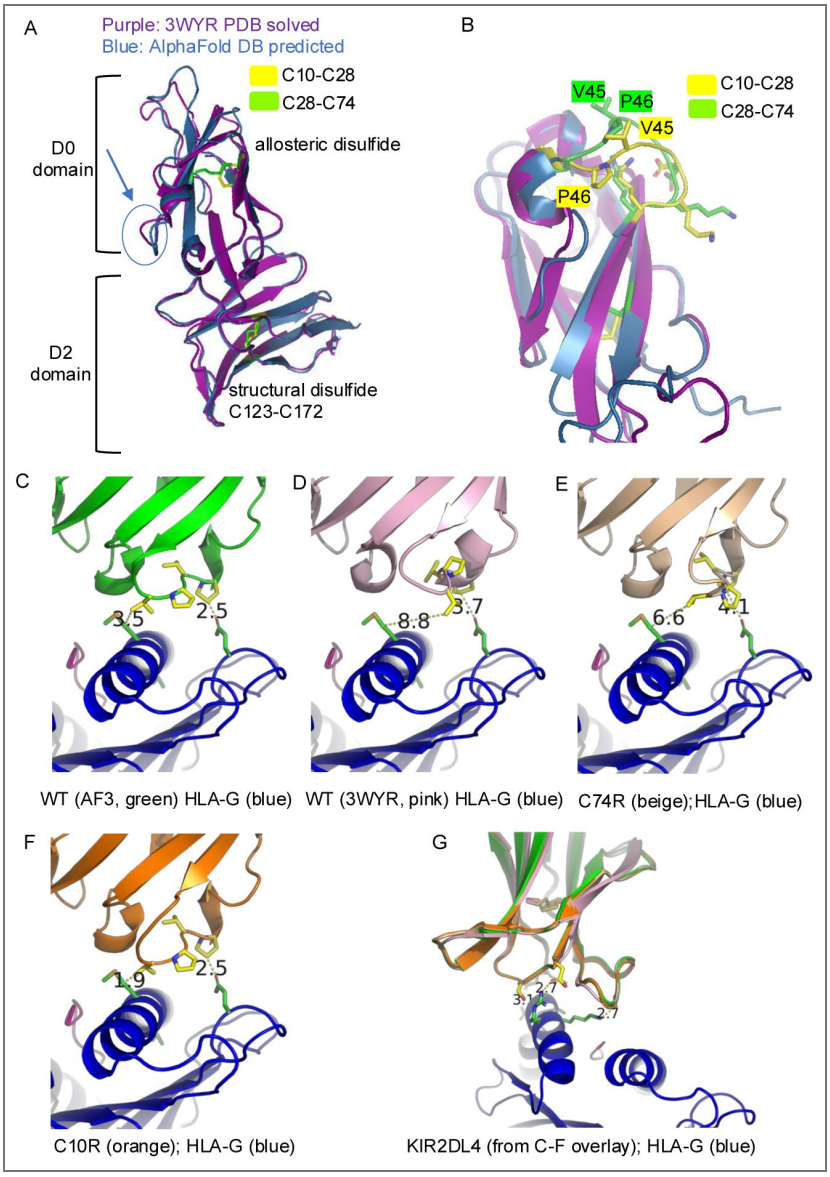

Figure 6. Predicted outcome of an allosteric disulfide switch on the conformation of KIR2DL4 and its interaction with HLA-G

(**A**) Overlay of the crystal structure (3WYR; *purple*) and the structure predicted by AlphaFold DB (*blue*). The allosteric disulfide Cys10-Cys28 is in yellow and the Cys28-Cys74 structural disulfide is in green. The circle indicated with a blue arrow shows the proline loop shown in B. (**B**) D0 domain shown with the Proline loop facing up and pointing toward the predicted HLA-G binding site. The position of Val45 and Pro46 in the crystal structure (C10-C28; *yellow*) is overlayed with that in the AlphaFold predicted structure (C28-C74; *green*). The distance between the Val45 and Pro46 in the crystal structure and their counterpart in the predicted structure of a Cys28-Cys74 structure is 5.3 and 5.4 Angstrom, respectively. (**C**) KIR2DL4 (*green*) D0 domain interaction with HLA-G (*blue*) as predicted by AlphaFold3. Val45 and Pro48 of KIR2DL4 contact Met76 and Glu19 in HLA-G, respectively. The numbers indicate the distance in Angstrom between side chains on KIR2DL4 (*yellow*) and side chains on HLA-G (*green*). (**D**) Docking of the KIR2DL4 crystal structure (3WYR, *pink*) and HLA-G (*blue*), as predicted by AlphaFold3. The shift of the Proline loop moves the side chains Val45 and Pro48 away to a distance greater than 3.5 Angstrom. (**E**) Predicted interaction of mutant KIR2DL4 C74R (*beige*) with HLA-G (*blue*). The structure of this KIR2DL4 in a Cys10-Cys28 configuration resembles that of the crystal structure, with distances greater than 3.5 Angstrom between side chains on C74R (*yellow*) and HLA-G (*green*). (**F**) Predicted interaction between the KIR2DL4 C10R AlphaFold DB structure (*orange*) and HLA-G (*blue*). This KIR2DL4 in a Cys28-Cys74 configuration resembles the WT KIR2DL4 (in C) and maintains close contacts with HLA-G via side chains Val45 and Pro48. (**G**) Predicted interaction of the four D2 Ig domains (shown as an overlay) with HLA-G (*blue*). Predicted close contacts of KIR2DL4 with HLA-G include the pairs Ser128–Arg145 (3.1 A, *left*), Asp130–Arg145 (2.7 A, *center*), and Ser179–Lys146 (2.7 A, *right*).

The predicted D2 domain contacts with HLA-G, which are similar to those of KIR2DL1 with HLA-Cw4, are unaffected by the disulfide switching, as seen in the overlay of D2 domains for all 4 structures, the crystal structure (3WYR) and AlphaFold predictions of wild-type, C74R, and C10R KIR2DL4 (Fig. 6G). Thus, the D2 domain contacts (Table S2, Fig. S3) are preserved regardless of the disulfide bond usage in the D0 domain. These results support the interpretation that allosteric changes induced by a switch from a Cys10-Cys28 disulfide bond to a canonical Cys28-Cys74 bond in KIR2DL4 changes the orientation of a distant loop in the D0 domain, such that it could now contact HLA-G (Movie S1).

Discussion

Transcription of *HLA-G* is turned on in fetal extravillous trophoblast (EVT) cells just as they reach the fetal-maternal interface during early pregnancy, concomitant with high transcription of several matrix metalloprotease genes (5), including *MMP2*, which can promote shedding of soluble HLA-G at the plasma membrane (26, 27). The abundant NK cells in the decidua are distinct from maternal blood NK cells (28) and have their own transcriptional signature, including high expression of *KIR2DL4* (5). As expected for cellular processes that support human reproduction, the encounter of EVT cells with decidual NK cells at the maternal-fetal interface is well orchestrated (5, 29). High transcription of *KIR2DL4* in decidual NK cells is matched by high and selective expression of HLA-G in EVT cells. Uptake of soluble HLA-G into cells depends on KIR2DL4 and both colocalize in Rab5$^+$ early endosomes from where signaling occurs (12). As a strong ligand for the inhibitory receptor LILRB1, which is selectively expressed by the dNK1 subset of decidual NK cells, HLA-G at the plasma membrane can provide protection to EVT cells. Another protective role of HLA-G occurs by the release of a peptide from its signal sequence that provides a strong ligand for the inhibitory receptor NKG2A (*KLRC1*) via presentation by HLA-E (30–32). Therefore, inhibitory signaling through LILRB1–HLA-G and NKG2A–HLA-E interactions protect EVT from NK killing. However, signaling from endosomes triggered by the interaction of soluble HLA-G with KIR2DL4 is protected from inhibition at the cell surface and induces secretory responses that support vascular remodeling and fetal growth.

To address the question of how KIR2DL4 interacts with HLA-G, a random mutagenesis approach was chosen to generate a library of mutant KIR2DL4 that were then tested for their ability to endocytose soluble HLA-G. This analysis revealed that binding of HLA-G and uptake of soluble HLA-G into endosomes was regulated by a trio of cysteine residues in the first Ig domain of KIR2DL4, called D0. In addition to the disulfide bond typical of Ig domains (Cys28-Cys74), such as the D0 domain of KIR2DL5 and KIR3DL1, a third cysteine is present at position 10 in KIR2DL4. The only KIR2DL4 structure reported so far has this atypical Cys10-Cys28 bond, leaving a free cysteine at position 74 (14). Our mutants of Cys74 revealed that a KIR2DL4 with a Cys10-Cys28 bond as the only option, was mainly in endosomes of transfected cells, like wild-type KIR2DL4, but neither bound HLA-G nor induced endocytosis of soluble HLA-G. Alternatively, mutations at Cys10, which left the D0 domain with a single disulfide bond (Cys28-Cys74), failed to internalize, leaving KIR2DL4 at the plasma membrane. Furthermore, in contrast to mutations at Cys74, mutants without Cys10 remained at the plasma membrane and their internalization into endosomes was induced by soluble HLA-G. Thus, proper KIR2DL4 function depends on a switch from one disulfide bond to another, keeping Cys28 as a common partner for either Cys10 or Cys74. We found that the Cys10-Cys28 bond has a –RHstaple conformation, which is a signature of allosteric bonds having an inherent high bond stress that predisposes it to cleavage (19). Here, we have shown that KIR2DL4 in human cells exists in both disulfide configurations, and that the allosteric Cys10-Cys28 bond is reduced in vitro by the thiol disulfide oxidoreductase PDI. As expected, if PDI activity is required to maintain a pool of Cys28-Cys74 KIR2DL4 at the plasma membrane (by reducing Cys10-Cys28 bonds), thiol blockade with membrane impermeable DTNB did inhibit HLA-G binding.

AlphaFold predictions of KIR2DL4 folding and interaction with HLA-G showed that a switch from Cys10-Cys28 to a Cys28-Cys74 disulfide bond would cause an allosteric shift in a distant loop in D0 and bring the Val45 to Pro48 loop in a position that permits interactions with Met76 and Glu19 of

HLA-G. The lack of reported detectable binding of purified KIR2DL4 with HLA-G in vitro (14) may be explained by the incompatibility of a Cys10-Cys28 bonded KIR2DL4 with HLA-G binding.

The regulation of a KIR2DL4–HLA-G interaction by an allosteric disulfide that controls protein conformation provides yet another example of disulfide bonds serving as switches in protein function. Allosteric disulfides regulate diverse biological processes, such as hemostasis (tissue factor, platelet fibrinogen receptor integrin αIIb-β3, and von Willebrand factor), and viral infection (gp120 of HIV-1) (15). Allosteric disulfide bonds specifically targeted by extracellular PDI at the cell surface have been identified in proteins such as GP1bα, tissue factor (*F3*), αvβ3 integrin during thrombosis, and HIV-1 envelope gp120 when bound to CD4 during viral entry (33, 34).

KIR2DL4, the only KIR family member expressed by all human NK cells, and highly transcribed in decidual NK cells, joins the list of proteins whose function is controlled by a labile disulfide bond acting as a switch, but here in the context of early pregnancy. In response to fetal HLA-G, NK cells endocytose soluble HLA-G bound to KIR2DL4, which signals from endosomes for a secretory response that leads to a sustained secretion of factors that support vascular remodeling and fetal development (4, 13). In addition, NK cells induce an ISG response upon interacting with HLA-G which protect NK cells from infections in early pregnancy (9). In this unique environment at the maternal fetal interface, the allosteric disulfides may act as a functional switch to regulate KIR2DL4 localization, binding to HLA-G and signaling to enable NK cells to support a successful pregnancy.

Materials and Methods

Cells and reagents

HEK293T cells (hereafter called 293T) were obtained from the American Type Culture Collection (ATCC) and cultured in Iscoves Modified Dulbecco's medium containing 10% fetal calf serum (FCS). KIR2DL4 and receptor 2B4 (*CD244*) were tagged at the N-terminus with the short YPYDVPDYA amino acid sequence (HA tag) present in the pDisplay expression vector. 293T–2DL4-gfp cells were generated as described (12). Briefly, 293T–2DL4-gfp cells were made by transfecting 293T cells using LipofectAMINE 2000, with a KIR2DL4 cDNA fused to green fluorescence protein (gfp) in the vector pBABE (puro) CMV^+ using SalI and BamH1 sites. Transfected cells were selected and maintained in Iscove's medium containing puromycin at a concentration of 2 mg/ml. Recombinant HLA-G and HLA-E were obtained from the Immune Monitoring Services, Fred Hutchinson Cancer Center (Seattle, WA). Briefly, MHC heavy chain protein and β2-microglobulin (β2m) were produced in *E. coli* and purified from inclusion bodies. The HLA-G heavy chain and b2m proteins were refolded *in vitro* in the presence of peptide KGPPAALTL into a monomeric peptide-MHC complex. For HLA-E, refolding was done in the presence of peptide VMAPRTLFL. Monomers of the refolded p-MHC were purified by FPLC using size exclusion chromatography and concentrated to 1 mg/mL. Soluble HLA-G and HLA-E were labeled using the Alexa Fluor 647 Protein Labeling Kit (Cat #: A20173, Molecular Probes, ThermoFisher). mAb#33 was produced in our laboratory (11) and MAB2238 was obtained from RnD Systems.

Random Mutagenesis Screen

Random mutagenesis of the KIR2DL4 sequence spanning amino acids 1-208, consisting of the Ig domains D0 and D2 and a portion of the stem was carried out using the Diversify PCR Random Mutagenesis kit (Clontech, Cat#630703) according to manufacturer's instructions. HA-tagged KIR2DL4 expressed in pDisplay served as the DNA template. The primers used at 10 mM for PCR were as follows: Sense: CCTGCTATGGGTACTGCTGCTCTGGGTTCC; Antisense: GAAGGGGAGGATGGT GAAGAGGATGATGGC. $Mn2^+$ (80 mM) and dGTP (40 mM) was used to obtain the desired mutation rate of 1 to 2 mutations per kb of DNA. Thermal cycling conditions consisted of denaturation at 94° for 30 sec, followed by annealing at 94°C for 30 sec and extension at 68°C for 1 min for a total of 25 cycles. Mutated KIR2DL4 was cloned back into pDisplay, and colonies were sequenced to select for single or double amino acid mutations. Each mutant (1 mg) was then transiently transfected into 293T cells using LipofectAMINE 2000 according to manufacturer's instructions. After 36 h, cells

were trypsinized and plated into 8 well glass chambers. Cells were plated at a density of 7 ξ 10^4 cells/well in eight-well coverglass slides (Nunc Lab-Tek, Thermo Fisher Scientific) 18 h prior to loading. Cells were then loaded with anti-HA Ab coupled to Alexa 594 (Biolegend) (0.03 mM) and HLA-G coupled to Alexa 647 (0.04 mM) for 2 h at 37°C. Cells were then washed in PBS and viewed by microscopy using a Zeiss 780 confocal microscope.

Confocal microscopy

Image acquisition was performed using a LSM 780 confocal laser scanning microscope (Zeiss) fitted with a LD C-Apochromat 40ξ/1.1 W Corr objective. Cells were incubated at 37°C in 5% CO_2 for the entire acquisition duration. The HFT 543 nm and 633 nm main beam splitters were used to detect signals from fluorophores Alexa-Fluor 594 and 647, respectively. Parameters were set to acquire at a fixed pixel density of 512 ξ 512, 16-bit pixel depth, and pinhole size of 100 mm. Images were processed and colocalization coefficients were calculated using the Zeiss ZEN software. Quantification of receptor and ligand localization was performed as follows. Transfected cells expressing fluorescently tagged proteins were viewed in a series of multiple fields using the LSM 780. Cells in each field were counted and categorized based on the location and ligand colocalization status of the expressed receptor. Counts were averaged over 2 to 4 experiments, and the number of cells counted per sample ranged from $100 \leq n \leq 430$. In a typical transfection with wild-type KIR2DL4, approximately 80% of the transfected cells had clear signals for internalized HLA-G and KIR2DL4 in the same endosomal compartments, and the remaining 20% had low but detectable 2DL4 at the plasma membrane but no HLA-G. Endosomes positive for 2DL4 but without an HLA-G signal were noted in less than 2% of the cells.

Thiol Blockade and PDI Inhibition Assays

In eight-well coverglass slides, 293T cells transfected with HA-2DL4 were preincubated in Iscoves media containing DTNB (5,5'-Dithiobis 2-nitrobenzoic acid; Sigma), pCMPS (para-chloromercuriphenylsulfonate; Carbosynth), Rutin (Sigma), or anti-PDI antibody RL90 (Thermo Fisher) at varying concentrations for 1 h at 37°C. Anti-HA-594 and HLA-G-647 were then added and incubated for 2 h in the continued presence of inhibitor at 37°C. Cells were then washed twice with PBS and analyzed by confocal microscopy as described above.

Quantification of cysteine redox states

GFP-tagged KIR2DL4 expressed in 293T cells was immunoprecipitated from cells using ChromTek-GFP Trap Agarose (Proteintech). Free thiols were labelled with 2-iodo-N-phenylacetamide (^{12}C-IPA) followed by cell lysis, immunoprecipitation of 2DL4-GPF and second ^{12}C-IPA labelling of proteins prior to elution. 2DL4-GFP immunoprecipitated from cells were analyzed on SDS-PAGE. Protein band corresponding to 2DL4-GFP (75 kDa) was detected from a single eluate prepared from cells and the gel area corresponding to 75 kDa was excised, reduced with dithiothreitol (DTT), and reduced thiols alkylated with ^{13}C-IPA. The redox states of cysteines were quantified by mass spectrometry analysis. Reactions were stopped by adding 5% (v/v) formic acid, and peptides were eluted from the gel slices with 5% formic acid and 50% (v/v) acetonitrile.

Peptides were desalted using Ziptip (Millipore), dried and reconstituted in 0.1% formic acid. Using a Thermo Fisher Scientific Ultimate 3000, peptides were injected and resolved on a 35cm × 75 mm C18 reverse phase analytical column with integrated emitter using a 2-35% acetonitrile over 22 min with a flow rate of 300 nL/min. The peptides were ionized by electrospray ionization at +2.0 kV. Tandem mass spectrometry analysis was carried out on a Q-Exactive Plus mass spectrometer (Thermo Fisher Scientific) using HCD fragmentation. The data-dependent acquisition method acquired MS/MS spectra of the top 5 most abundant ions at any one point during the gradient. The data was searched using Mascot (Matrix Science) against Uniprot database. Search parameters were as follows: precursor tolerance of 6 ppm and product ion tolerances of ± 0.4 Da. Oxidized Met, pyro-Glu and pyro-Gln were selected as variable modifications with full chymotryptic cleavage of up to three missed cleavages. To calculate ion abundance of peptides, extracted ion chromatograms were generated using the XCalibur Qual Browser software (v2.1.0; Thermo

Scientific). The area was calculated using the automated peak detection function built into the software. Abundance of disulfide-linked peptides was expressed as a ratio relative to disulfide-linked peptide between Cys123-Cys172 in the D2 domain. Disulfide bond analysis was performed using the Disulfide bond Analysis Tool.

Recombinant KIR2DL4 protein (WT, C10S and C74S) were produced in insect cells and purified by His-tag affinity chromatography. The extracellular domain of KIR2DL4*001 (residues 1-195) was subcloned into the pAC insect expression vector in frame with an N-terminal 8× HisTag and a 3C protease cleavage site. The KIR2DL4 expression vector was then transfected with BestBac 2.0 linearized DNA (Expression Systems) into Sf9 cells to generate P1 virus. Virus was amplified by shaking culture in Sf9 cells prior to expression. KIR2DL4 was then expressed in BTI-Tn-5B1-4 insect cells (High Five) and purified using Ni-NTA affinity purification followed by Superdex 200 size exclusion into 10 mM HEPES, 150 mM NaCl, pH 7.2. Fractions containing the purified protein were verified by SDS-PAGE. Recombinant thiol isomerases (PDI, ERp57 and thioredoxin) were expressed in *E. coli* and purified by His-tag affinity chromatography. The thiol isomerases were then reduced with final 10 mM dithiothreitol for 30 min at 25°C and desalted into PBS using a Zeba spin column (Themo Fisher Scientific). KIR2DL4 (3 mg) was treated with either a 2- or a 10-fold molar excess of each thiol isomerase for 30 min at 25°C. Free thiols in 2DL4 were alkylated with 5 mM 2-iodo-N-phenylacetamide (^{12}C-IPA) and the protein was resolved on non-reducing SDS-PAGE, stained with Bio-Safe Coomassie stain and destained in deionized water. Bands corresponding to 2DL4 were excised, dried, incubated with 40 mM dithiothreitol and washed. The fully reduced proteins were alkylated with 5 mM ^{13}C-IPA. The gel slices were washed and dried before digestion of proteins with 12 ng/mL of chymotrypsin (Roche) in 25 mM NH4CO2 containing 10 mM CaCl2 overnight at 25°C. Peptides were eluted from the slices with 5% formic acid, 50% acetonitrile. Peptides were desalted using Ziptips (Merck Millipore). Liquid chromatography, mass spectrometry and data analysis were performed as described (35, 36). The fraction of reduced disulfide bond was measured from the relative ion abundance of peptides containing ^{12}C-IPA and ^{13}C-IPA. To calculate ion abundance of peptides, extracted ion chromatograms were generated using the XCalibur Qual Browser software (v2.1.0; Thermo Fisher Scientific). The area was calculated using the automated peak detection function built into the software. The ratio of ^{12}C-IPA and ^{13}C-IPA alkylation represents the fraction of the cysteine in the population that is in the reduced state (35).

Site directed mutagenesis

Engineered mutations of KIR2DL4 in the pDisplay vector were carried out using the QuikChange site directed mutagenesis kit (Stratagene) according to the manufacturer's instructions. Mutations were verified by sequencing. Stable transfections of cysteine mutants of KIR2DL4 were carried out using Lipofectamine 2000 according to the manufacturer's instructions and selected using 1 mg/ml puromycin. Transfected cells were sorted by flow cytometry to generate transfectants with uniform expression of the HA-tag.

Data availability

All data generated or analyzed during this study are included in the manuscript and supporting files

Supplementary figures and tables

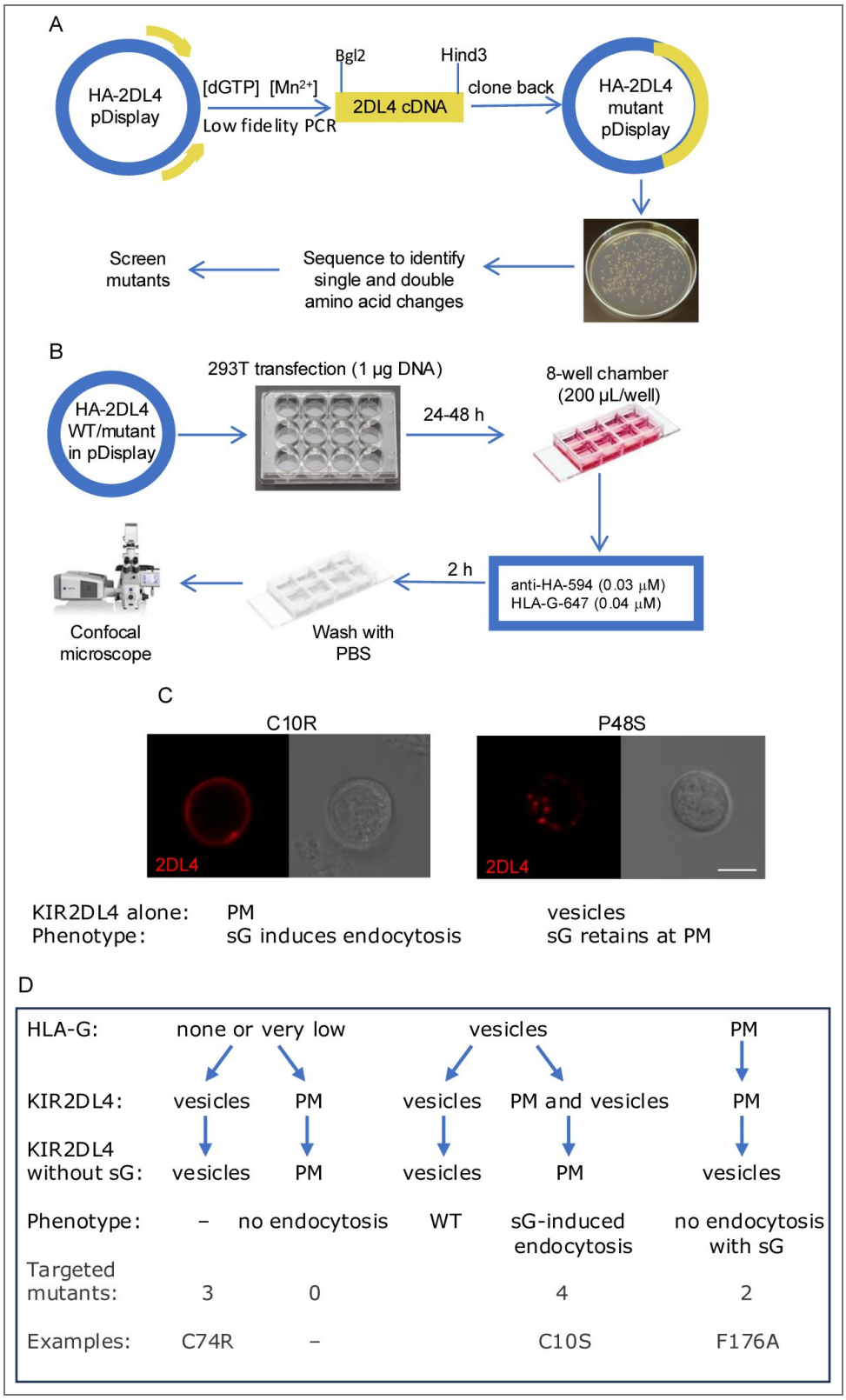

Fig. S1. Random mutagenesis screen. (**A**) Generation of mutants. (**B**) Analysis of mutants by confocal microscopy. (**C**) In the same assay shown in Figure 1C, mutants C10R and P48S were tested in the absence of HLA-G. Confocal images of anti-HA-Alexa-594 revealed their location (first panel). A DIC image is shown in the

right. (**D**) Flow chart of mutants distributed among 4 categories distinct from WT. Several mutants from each category were also tested in the absence of soluble HLA-G. The location of KIR2DL4 often depends on HLA-G. For example, C10R was not internalized and P48S was able to internalize into vesicles in the absence of soluble HLA-G.

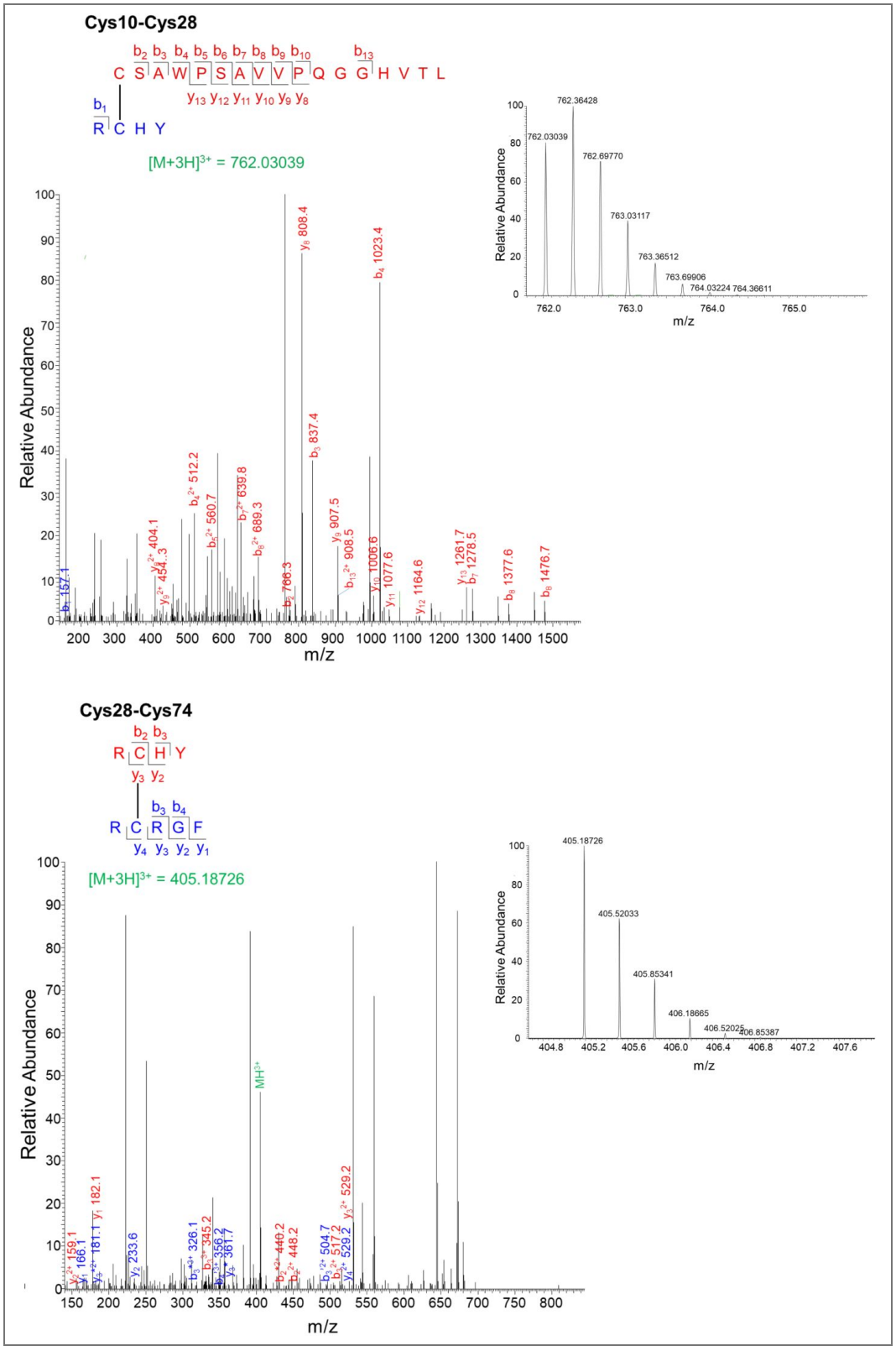

Fig. S2. Disulfide-linked peptide analysis of recombinant KIR2DL4 protein by mass spectrometry.

Tandem mass spectra of the peptides linked by disulfide bond between Cys10 and Cys28 and between Cys28 and Cys74 are shown. The accurate mass of Cys10-Cys28 and Cys28-C74 peptides are shown in the insets (Cys10-Cys28: [M + 3H]3+ = *m/z* 762.03039 and expected [M + 3H]3+ = *m/z* 762.0299; Cys28-Cys74 : [M + 3H]3+ = *m/z* 405.18726 and expected [M + 3H]3+ = *m/z* 405.1870). Ions with a neutral loss of small molecules are labelled with an asterisk (loss of ammonia) and a prime (loss of water).

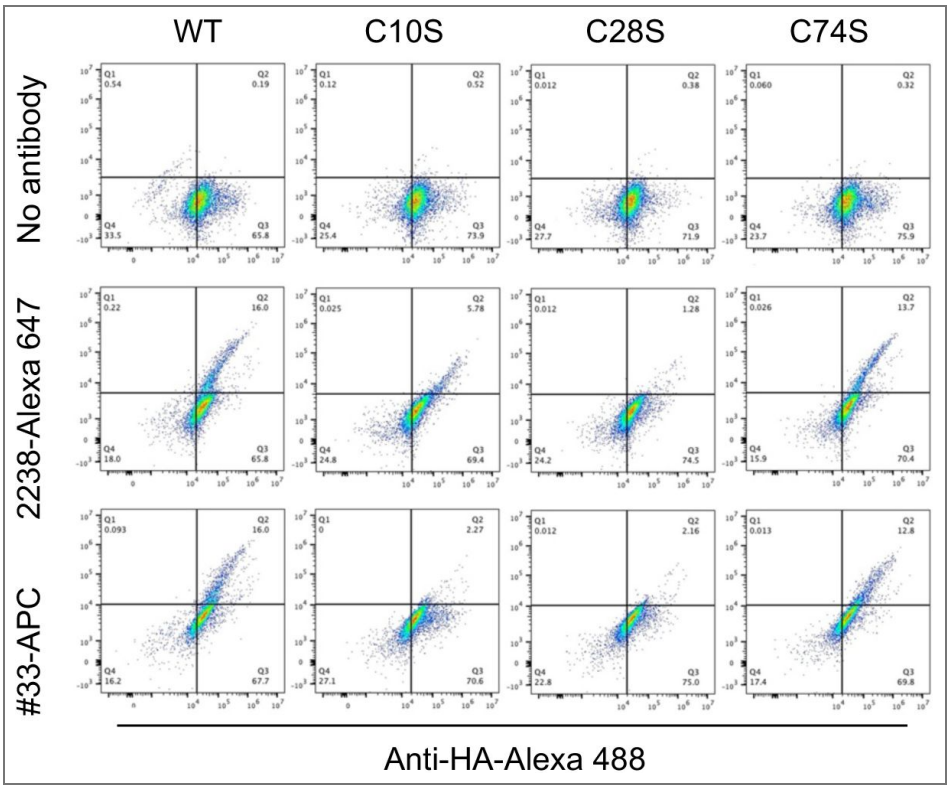

Fig. S3. Flow cytometry profiles of 293T cells expressing HA-tagged KIR2DL4 WT and, in parallel, the 3 Cys to Ser mutants loaded for 2 h at 37°C with antibodies to the HA-tag and KIR2DL4.

Staining with the control anti-HA antibody coupled with Alexa 488 is shown on the x axis versus no antibody (*top*), MAB2238-Alexa 647 (*center*), and mAb #33-APC (*bottom*) on the y axis. The lower left quadrant was set to include and gate out 98% of unstained control cells.

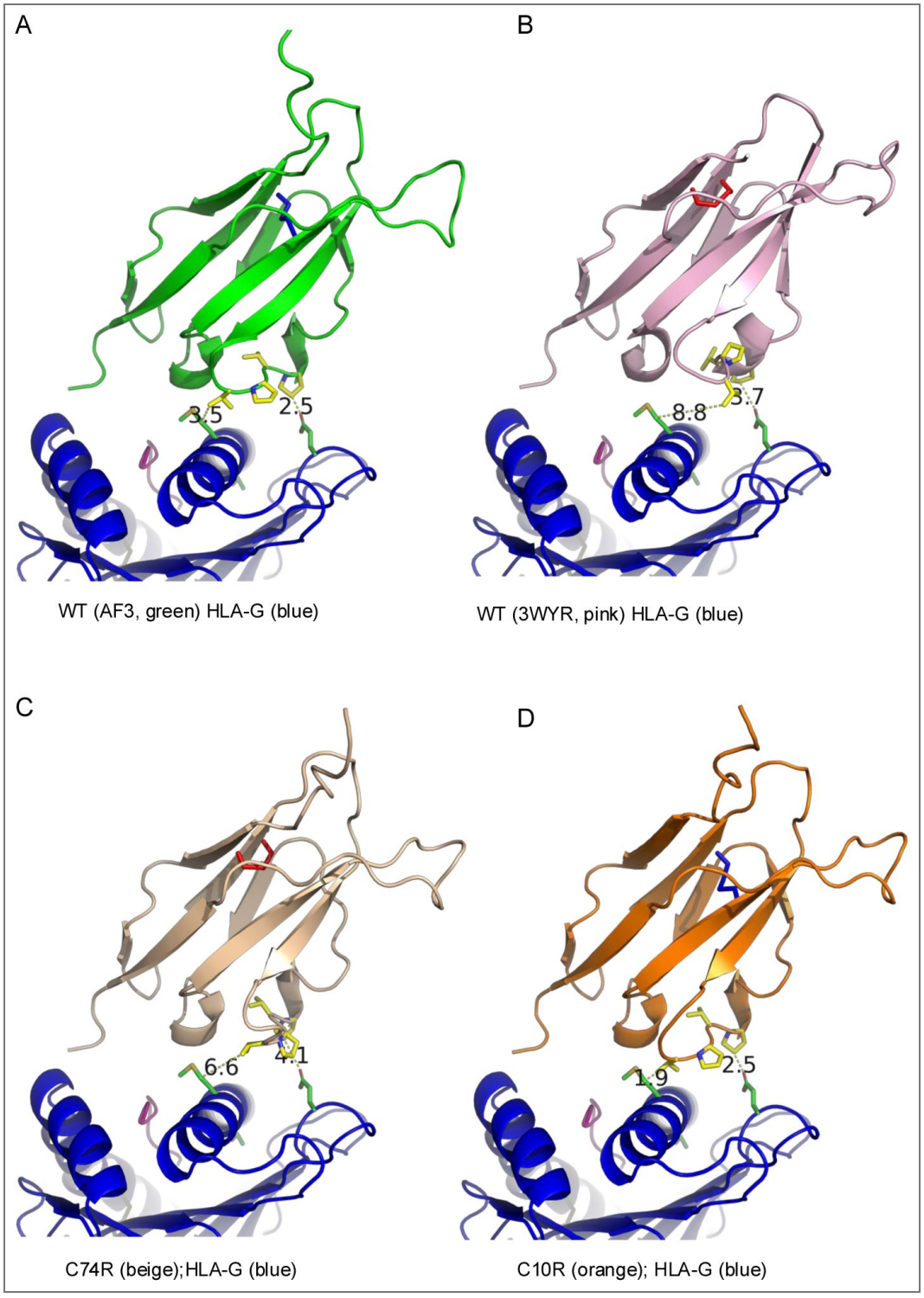

Fig. S4. Full images of the D0 domains shown in Figure 6 (C-F).

The Cys28-Cys74 disulfide bond is shown in blue (A, D).The Cys10-Cys28 disulfide bond is shown in red (B, C).

Cys	Peptide sequence*	Peptide score#	Peptide error (ppm)
10	**C**SAWPSAVVPQGGHVTL **C**SAWPSAVVPQGGH **C**SAW	549.9 403.3 351.1	0.16 0.8 0.8
28	R**C**HY	255.5	0.3
74	R**C**RGF	245.7	0.72
123	S**C**SSQSSF S**C**SSQSSFDIY	383.9 387.2	0.97 0.32
172	R**C**FGSF	367.9	0.91

*Cys was labelled with ^{12}C-iodoacetanilide or ^{13}C-iodoacetanilide and is in bold.
#Peptide score calculated by Byonic analysis software is a primary indicator of peptide-spectrum matches.

Table S1. 2DL4 peptides analyzed to determine disulfide bond redox state.

Peptides were detected by Byonic analysis software, confirmed by MS/MS and have errors <6 ppm. Only peptides with peak areas >10 million for a given Cys were included in the analysis.

KIR2DL4	HLA-G	Type
Val 45^{CG2}	Met76^{CG}	VDW
Pro 48^{CB}	Glu19^{OE1}	VDW
Pro 48^{CG}	Glu19^{OE1}	VDW
Leu 99^{O}	Ala150^{CB}	VDW
Tyr 100^{CA}	Ala149^{O}	VDW
Tyr 100^{CB}	Ala149^{O}	VDW
Glu 101^{N}	Ala149^{O}	H-bond
Glu101^{OE1}	Asn151^{CB}	VDW
Glu101^{OE1}	Asn151^{ND2}	H-bond
Ser128^{C}	Arg145^{NH2}	VDW
Ser128^{O}	Arg145^{NE}	H-bond
Ser128^{O}	Arg145^{CZ}	VDW
Ser128^{O}	Arg145^{NH2}	H-bond
Ser128^{OG}	Arg145^{CG}	VDW
Ser128^{OG}	Arg145^{NE}	H-bond
Asp130^{OG}	Arg145^{NH2}	VDW
Asp130^{OD1}	Arg145^{CZ}	VDW
Asp130^{OD1}	Arg145^{NH1}	Salt bridge
Asp130^{OD1}	Arg145^{NH2}	Salt bridge
Ser179^{OG}	Lys146^{NZ}	H-bond

Atomic contacts determined with PYMOL.
Van der Waal interactions defined as nonhydrogen bond contact distances of 3.5 A or less.
Hydrogen bond interactions are defined as contact distances of 3.5A or less.
Salt bridge is defined as contact distance of 3.5A or less.

Table S2. Contacts between KIR2DL4 and HLA-G in AlphaFold3 structure of KIR2DL4.

Acknowledgements

The contributions of the NIH authors were made as part of their official duties as NIH federal employees, are in compliance with agency policy requirements, and are considered Works of the United States Government. However, the findings and conclusions presented in this paper are those of the authors and do not necessarily reflect the views of the NIH or the U.S. Department of Health and Human Services.

Additional information

Author Contributions

S.R., P.J.H. and E.O.L. designed research; S.R., G.M.M., J.C., J.L, S.M., and K.N. performed research; S.R., G.M.M, J.C., J.L., P.J.H. and E.O.L. analyzed data; S.R. and E.O.L. wrote the paper; S.R., J.C., P.J.H., E.O.L. edited the paper; E.J.A., P.D.S., P.J.H, and E.O.L. acquired funding.

Funding

Funder	Grant reference number	Author
HHS | NIH | NIDA | Intramural Research Program (IRP)	ZIA AI000525	Eric Long Peter D Sun
HHS | NIH | National Institute of Allergy and Infectious Diseases (NIAID)	RO1 AI170952	Erin J Adams
Government of New South Wales		Phillip J Hogg

Author ORCID iDs

Sumati Rajagopalan: https://orcid.org/0009-0002-7690-2767
Erin J Adams: https://orcid.org/0000-0002-6271-8574
Eric O Long: https://orcid.org/0000-0002-7793-3728

Additional files

Dataset S1

Video 1

References

1. **Parham P.,** Guethlein L. A. (2018) Genetics of Natural Killer Cells in Human Health, Disease, and Survival. *Annu Rev Immunol* **36**:519-548 https://doi.org/10.1146/annurev-immunol-042617-053149 | PubMed
2. **Cerwenka A.,** Lanier L. L. (2016) Natural killer cell memory in infection, inflammation and cancer. *Nat Rev Immunol* **16**:112-123 https://doi.org/10.1038/nri.2015.9 | PubMed
3. **Parham P.,** MoOett A. (2013) Variable NK cell receptors and their MHC class I ligands in immunity, reproduction and human evolution. *Nat Rev Immunol* **13**:133-144 https://doi.org/10.1038/nri3370 | PubMed
4. **Rajagopalan S.,** Long E. O. (2012) Cellular senescence induced by CD158d reprograms natural killer cells to promote vascular remodeling. *Proc Natl Acad Sci U S A* **109**:20596-20601 https://doi.org/10.1073/pnas.1208248109 | PubMed
5. **Vento-Tormo R.,** et al. (2018) Single-cell reconstruction of the early maternal-fetal interface in humans. *Nature* **563**:347-353 https://doi.org/10.1038/s41586-018-0698-6 | PubMed
6. **Li Q.,** et al. (2024) Human uterine natural killer cells regulate diOerentiation of extravillous trophoblast early in pregnancy. *Cell Stem Cell* **31**:181-195 e189 https://doi.org/10.1016/j.stem.2023.12.013 | PubMed

7. **Long E. O.,** Kim H. S., Liu D., Peterson M. E., Rajagopalan S. (2013) Controlling natural killer cell responses: integration of signals for activation and inhibition. *Annu Rev Immunol* **31**:227-258 https://doi.org/10.1146/annurev-immunol-020711-075005 | PubMed

8. **Rajagopalan S.,** Long E. O. (2012) KIR2DL4 (CD158d): An activation receptor for HLA-G. *Frontiers in immunology* **3**:258 https://doi.org/10.3389/fimmu.2012.00258 | PubMed

9. **Rajagopalan S.,** et al. (2026) The fetal trophoblast cell marker HLA-G activates a type I interferon response in primary NK cells through the receptor KIR2DL4. *Sci Signal* **19**:eadv2400 https://doi.org/10.1126/scisignal.adv2400 | PubMed

10. **Rajagopalan S.** (2010) Endosomal signaling and a novel pathway defined by the natural killer receptor KIR2DL4 (CD158d). *Tra=ic* **11**:1381-1390 https://doi.org/10.1111/j.1600-0854.2010.01112.x | PubMed

11. **Rajagopalan S.,** Fu J., Long E. O. (2001) Cutting edge: induction of IFN-gamma production but not cytotoxicity by the killer cell Ig-like receptor KIR2DL4 (CD158d) in resting NK cells. *J Immunol* **167**:1877-1881 https://doi.org/10.4049/jimmunol.167.4.1877 | PubMed

12. **Rajagopalan S.,** et al. (2006) Activation of NK cells by an endocytosed receptor for soluble HLA-G. *PLoS Biol* **4**:e9 https://doi.org/10.1371/journal.pbio.0040009 | PubMed

13. **Rajagopalan S.,** Moyle M. W., Joosten I., Long E. O. (2010) DNA-PKcs controls an endosomal signaling pathway for a proinflammatory response by natural killer cells. *Sci Signal* **3**:ra14 https://doi.org/10.1126/scisignal.2000467 | PubMed

14. **Moradi S.,** et al. (2015) The structure of the atypical killer cell immunoglobulin-like receptor, KIR2DL4. *J Biol Chem* **290**:10460-10471 https://doi.org/10.1074/jbc.m114.612291 | PubMed

15. **Chiu J.,** Hogg P. J. (2019) Allosteric disulfides: Sophisticated molecular structures enabling flexible protein regulation. *J Biol Chem* **294**:2949-2960 https://doi.org/10.1074/jbc.rev118.005604 | PubMed

16. **Zhou B.,** Baldus I. B., Li W., Edwards S. A., Grater F. (2014) Identification of allosteric disulfides from prestress analysis. *Biophys J* **107**:672-681 https://doi.org/10.1016/j.bpj.2014.06.025 | PubMed

17. **Vivian J. P.,** et al. (2011) Killer cell immunoglobulin-like receptor 3DL1-mediated recognition of human leukocyte antigen B. *Nature* **479**:401-405 https://doi.org/10.1038/nature10517 | PubMed

18. **Schmidt B.,** Ho L., Hogg P. J. (2006) Allosteric disulfide bonds. *Biochemistry* **45**:7429-7433 https://doi.org/10.1021/bi0603064 | PubMed

19. **Pijning A. E.,** Chiu J., Yeo R. X., Wong J. W. H., Hogg P. J. (2018) Identification of allosteric disulfides from labile bonds in X-ray structures. *R Soc Open Sci* **5**:171058 https://doi.org/10.1098/rsos.171058 | PubMed

20. **Jasuja R.,** et al. (2012) Protein disulfide isomerase inhibitors constitute a new class of antithrombotic agents. *J Clin Invest* **122**:2104-2113 https://doi.org/10.1172/jci61228 | PubMed

21. **Varadi M.,** et al. (2024) AlphaFold Protein Structure Database in 2024: providing structure coverage for over 214 million protein sequences. *Nucleic Acids Res* **52**:D368-D375 https://doi.org/10.1093/nar/gkad1011 | PubMed

22. **Jumper J.,** et al. (2021) Highly accurate protein structure prediction with AlphaFold. *Nature* **596**:583-589 https://doi.org/10.1038/s41586-021-03819-2 | PubMed

23. **Boyington J. C.,** Motyka S. A., Schuck P., Brooks A. G., Sun P. D. (2000) Crystal structure of an NK cell immunoglobulin-like receptor in complex with its class I MHC ligand. *Nature* **405**:537-543 https://doi.org/10.1038/35014520 | PubMed

24. **Fan Q. R.,** Long E. O., Wiley D. C. (2001) Crystal structure of the human natural killer cell inhibitory receptor KIR2DL1-HLA-Cw4 complex. *Nat Immunol* **2**:452-460 https://doi.org/10.1038/87766 | PubMed

25. **Clements C. S.,** et al. (2005) Crystal structure of HLA-G: A nonclassical MHC class I molecule expressed at the fetal-maternal interface. *Proc Natl Acad Sci USA* **102**:3360-3365 https://doi.org/10.1073/pnas.0409676102 | PubMed

26. **Rizzo R.,** et al. (2013) Matrix metalloproteinase-2 (MMP-2) generates soluble HLA-G1 by cell surface proteolytic shedding. *Mol Cell Biochem* **381**:243-255 https://doi.org/10.1007/s11010-013-1708-5 | PubMed

27. **Park G. M.,** et al. (2004) Soluble HLA-G generated by proteolytic shedding inhibits NK-mediated cell lysis. *Biochem Biophys Res Commun* **313**:606-611 https://doi.org/10.1016/j.bbrc.2003.11.153 | PubMed

28. **Male V.,** MoOett A. (2023) Natural Killer Cells in the Human Uterine Mucosa. *Annu Rev Immunol* **41**:127-151 https://doi.org/10.1146/annurev-immunol-102119-075119 | PubMed

29. **MoOett A.,** Shreeve N. (2023) Local immune recognition of trophoblast in early human pregnancy: controversies and questions. *Nat Rev Immunol* **23**:222-235 https://doi.org/10.1038/s41577-022-00777-2 | PubMed

30. **Llano M.,** et al. (1998) HLA-E-bound peptides influence recognition by inhibitory and triggering CD94/NKG2 receptors: preferential response to an HLA-G-derived nonamer. *Eur J Immunol* **28**:2854-2863 https://doi.org/10.1002/(sici)1521-4141(199809)28:09<2854::aid-immu2854>3.0.co;2-w | PubMed

31. **Lee N.,** Goodlett D. R., Ishitani A., Marquardt H., Geraghty D. E. (1998) HLA-E surface expression depends on binding of TAP-dependent peptides derived from certain HLA class I signal sequences. *J Immunol* **160**:4951-4960 https://doi.org/10.4049/jimmunol.160.10.4951 | PubMed

32. **Borrego F.,** Ulbrecht M., Weiss E. H., Coligan J. E., Brooks A. G. (1998) Recognition of human histocompatibility leukocyte antigen (HLA)-E complexed with HLA class I signal sequence-derived peptides by CD94/NKG2 confers protection from natural killer cell-mediated lysis. *J Exp Med* **187**:813-818 https://doi.org/10.1084/jem.187.5.813 | PubMed

33. **Chiu J.,** Passam F., Butera D., Hogg P. J. (2015) Protein Disulfide Isomerase in Thrombosis. *Semin Thromb Hemost* **41**:765-773 https://doi.org/10.1055/s-0035-1564047 | PubMed

34. **Matthias L. J.,** et al. (2002) Disulfide exchange in domain 2 of CD4 is required for entry of HIV-1. *Nat Immunol* **3**:727-732 https://doi.org/10.1038/ni815 | PubMed

35. **Chiu J.** (2019) Quantification of the Redox State of Protein Disulphide Bonds. *Methods Mol Biol* **1967**:45-63 https://doi.org/10.1007/978-1-4939-9187-7_4 | PubMed

36. **Passam F. J.,** Chiu J. (2019) Allosteric disulphide bonds as reversible mechano-sensitive switches that control protein functions in the vasculature. *Biophys Rev* **11**:419-430 https://doi.org/10.1007/s12551-019-00543-0 | PubMed

Peer reviews

Reviewer #1 (Public review):

Summary:

This paper asks how the NK cell receptor KIR2DL4 binds HLA-G and undergoes endocytosis. The authors propose that an allosteric disulfide-bond switch controls whether the receptor is in a ligand-binding or non-binding state, and they support this model using mutagenesis, imaging, mass spectrometry, and structural prediction.

Strengths:

A major strength is the use of diverse, complementary approaches to validate the central claim. The authors combined unbiased random mutagenesis to identify key residues, confocal microscopy to track cellular localization , and mass spectrometry to quantify the redox states of specific disulfide bonds. These methods consistently support a single model: an allosteric disulfide switch. The transition between a Cys10-Cys28 bond and a Cys28-Cys74 bond serves as a functional switch that controls whether the receptor resides at the plasma membrane to bind ligand or remains inactive in endosomes.

Weaknesses:

The core model is interesting, but some of the strongest mechanistic claims still rely heavily on structure prediction rather than direct structural evidence, especially the proposed HLA-G contact surface in Figure 6.

The paper supports an effect of the disulfide state on trafficking and uptake, but the case for direct KIR2DL4-HLA-G binding still feels somewhat indirect. The manuscript itself notes that direct binding had not been previously shown, and the current explanation partly depends on inference about which disulfide state is present.

Most of the main experiments are done in transfected 293T cells, so it is still not fully clear how strongly this mechanism carries over to the more relevant NK-cell setting discussed in the paper.

The cellular evidence for the PDI story is not specific, since it depends a lot on inhibitor and blocking experiments that could affect the broader extracellular redox environment.

https://doi.org/10.7554/eLife.111018.1.sa1

Reviewer #2 (Public review):

Summary:

Rajagopalan et al show how extracellular domain features regulate KIR2DL4 internalization. The trafficking phenotypes of cysteine mutants are logically organized, and well-summarized in a Table. The disulfide mapping and differential alkylation strategy are appropriate and provide strong support for alternative disulfide configurations in D0. The higher accessibility or more selective reduction of Cys10-Cys28 as compared to Cys28-Cys74 by PDI is a key mechanistic anchor.

Strengths:

The identification of a conformational switch in KIR2DL4 is conceptually novel. Experimental elegance, detailed and well-written.

Weaknesses:

Most of the mechanistic work was shown in HEK293. The authors should exhibit relevance using primary NK cells (using primary NK)

https://doi.org/10.7554/eLife.111018.1.sa0